

## Thermodynamic Analysis on the Performance of Barocaloric Refrigeration Systems Using Neopentyl Glycol as the Refrigerant

DAI Zhaofeng<sup>1</sup>, SHE Xiaohui<sup>2,4</sup>, WANG Chen<sup>1,4</sup>, DING Yulong<sup>2</sup>, ZHANG Xiaosong<sup>1,3\*</sup>, ZHAO Dongliang<sup>1,3\*</sup>

1. School of Energy & Environment, Southeast University, Nanjing 210096, China

2. Birmingham Centre for Energy Storage, School of Chemical Engineering, University of Birmingham, Birmingham B15 2TT, UK

3. Engineering Research Centre of Building Equipment, Energy, and Environment, Ministry of Education, Nanjing 210096, China

4. School of Mechanical Engineering, Shijiazhuang Tiedao University, Shijiazhuang 050043, China

© Science Press, Institute of Engineering Thermophysics, CAS and Springer-Verlag GmbH Germany, part of Springer Nature 2023

**Abstract:** Barocaloric refrigeration is regarded as one of the next-generation alternative refrigeration technology due to its environmental friendliness. In recent years, many researchers have been devoted to finding materials with colossal barocaloric effects, while neglecting the research on barocaloric refrigeration devices and thermodynamic cycles. Neopentyl glycol is regarded as one of the potential refrigerants for barocaloric refrigeration due to its giant isothermal entropy changes and relatively low operating pressure. To evaluate the performance of the barocaloric system using Neopentyl glycol, for the first time, this study establishes a thermodynamic cycle based on the metastable temperature-entropy diagram. The performance of the proposed system is investigated from the aspects of irreversibility, operating temperature range, and operating pressure, and optimized with finite-rate heat transfer. The guidance for the optimal design of the system is given by revealing the effect of the irreversibility in two isobaric processes. The results show that a COP of 8.8 can be achieved at a temperature span of 10 K when the system fully uses the phase transition region of Neopentyl glycol, while a COP of 3 can be achieved at a temperature span of 10 K when the system operates at room temperature. Furthermore, this study also shows that the system performance can be further improved through the modification of Neopentyl glycol, and some future development guidance is provided.

**Keywords:** barocaloric refrigeration, neopentyl glycol, thermodynamic analysis, COP, refrigeration capacity

### 1. Introduction

Nowadays, vapor compression refrigeration technology has accounted for about 80% of the refrigeration market share [1]. However, the global warming potential (GWP)

of most traditional refrigerants in vapor compression refrigeration technology is 150 times higher than CO<sub>2</sub>, some even up to 8590 times [2, 3]. To address this challenge, the search of Low-GWP (GWP<150) refrigerants (e.g., natural refrigerants, hydrocarbons,

Received: Dec 2, 2021  
AE: WANG Lin

Corresponding author: ZHANG Xiaosong;  
ZHAO Dongliang

E-mail: rachpe@seu.edu.cn  
dongliang\_zhao@seu.edu.cn  
[www.springerlink.com](http://www.springerlink.com)

## Nomenclature

$A$	area of heat exchange/m <sup>2</sup>	$e$	expansion
COP	coefficient of performance	$H$	heat sink/heating
$h$	heat transfer coefficient/W·m <sup>-2</sup> ·K <sup>-1</sup>	$L$	heat source/cooling
$p$	operating pressure/MPa	max	maximum
$Q$	amount of heat exchanged/J	$p$	isobaric
$R$	refrigeration capacity/W	$r$	reversible
$s$	specific entropy/J·kg <sup>-1</sup> ·K <sup>-1</sup>	1–4	state of the barocaloric refrigeration cycle
$T$	temperature/K	1st	the 1st phase transition point
$t$	time/s	2nd	the 2nd phase transition point
$W$	mechanical work/J	3rd	the 3rd phase transition point
$0$	atmospheric pressure/MPa	4th	the 4th phase transition point
<b>Greek symbols</b>		a1–h1	change of state 1
$\Delta$	difference	a2–l2	change of state 2
$\eta$	adiabatic irreversibility-factor	a3–d3	change of state 3
<b>Subscripts</b>		a4–d4	change of state 4
ad	adiabatic	<b>Superscript</b>	
c	compression	*	dimensionless

hydrofluorocarbons) [4] and research on new refrigeration technologies (e.g., solid-state refrigeration) [5] have become two important directions. Among them, solid-state refrigeration technologies are gaining increasing attention due to their environmental friendliness, which include thermoelectric cooling [6], magnetocaloric cooling [7], electrocaloric cooling [8], elastocaloric cooling [9], and barocaloric cooling [10].

Thermoelectric cooling is based on the Peltier-Seebeck effect, which is only applicable to the cases requiring high reliability and small cooling capacity [11] because of the low energy conversion efficiency of thermoelectric materials [12]. Magnetic refrigeration based on the magnetocaloric effect has been studied widely [13]. However, its large-scale application is limited by the huge magnetic fields [14] and the high cost of permanent magnets [15]. Electrocaloric cooling is based on the material's polarization during the change of the electric field [16], which has undergone rapid development recently. Nevertheless, the isothermal entropy change and adiabatic temperature change produced by electrocaloric cooling are small [17]. And, electrocaloric materials have drawbacks of easy breakdown, difficult processing [18], and short fatigue life [19]. The current elastocaloric cooling technology is mainly based on the martensitic phase transition of shape memory alloys (SMAs) under stress [20], but of course other materials such as rubber can also be used for elastocaloric cooling [21]. At present, Ni-Ti shape-memory alloy is the most widely used material [22], but it has a serious drawback of short fatigue life. The barocaloric effect is characterized by isothermal

entropy or adiabatic temperature change in a solid-state substance when an hydrostatic pressure is applied or withdrawn [23]. In 2010, Manosa et al. reported the barocaloric effect in Ni-Mn-In magnetic shape-memory alloy [24]. After that, barocaloric effect was also found in some magnetocaloric materials, including LaFe<sub>11.33</sub>Co<sub>0.47</sub>Si<sub>1.2</sub> alloy [25], Gd<sub>5</sub>Si<sub>2</sub>Ge<sub>2</sub> [26], Fe<sub>49</sub>Rh<sub>51</sub> [27], Mn<sub>3</sub>GaN [28]. In 2017, Bermúdez-García et al. found the barocaloric effect in organic-inorganic hybrid perovskites [29], and Aznar et al. studied the barocaloric effects in superionic conductor AgI [30]. Nevertheless, the isothermal entropy change of these materials is so small that it is difficult to achieve a large refrigeration capacity.

Recently, materials with giant barocaloric effects have been discovered one after another. Romanini et al. reported that Fe<sub>3</sub>(bntz)<sub>6</sub>(tcnset)<sub>6</sub> can reach an entropy change of 120 J·kg<sup>-1</sup>·K<sup>-1</sup> under 260 MPa [31]. Li et al. found that (C<sub>10</sub>H<sub>21</sub>NH<sub>3</sub>)<sub>2</sub>MnCl<sub>4</sub> can reach an entropy change of 230 J·kg<sup>-1</sup>·K<sup>-1</sup> under 50 MPa [32]. Unfortunately, to date, almost all research articles related to barocaloric refrigeration have been limited to the exploration of barocaloric materials [33, 24]. Nevertheless, these discovered materials are not comparable to the colossal entropy change found in plastic crystals [10]. Plastic crystals offer the advantages of high compressibility, low driving force, and low cost, making them ideal for barocaloric refrigeration. Neopentyl glycol (NPG) is the plastic crystal phase transition temperature closest to room temperature, which can obtain a colossal entropy change of 389 J/(kg·K) under 45 MPa [35]. Because of its great potential,

Lloveras et al. investigated the barocaloric effect of NPG under higher hydrostatic pressure [36]. Aznar et al. investigated the minimum hydrostatic pressure required to achieve reversible barocaloric effects for four plastic crystals [37]. However, no studies have been conducted to evaluate the performance of the barocaloric system using NPG as the refrigerant, and this is almost a gap in research on other barocaloric materials. Only Aprea et al. established an active caloric refrigerator using a 2D model [38] and investigated the performance of the barocaloric system with different heat transfer fluids [39]. Nevertheless, their research calculates the barocaloric effect indirectly using the temperature change to calculate the entropy change, which deviates from the actual measurement [40]. Therefore, there is no simple and direct method to predict the performance of the barocaloric refrigeration system at present. Magnetic refrigeration, also a solid refrigeration technology, has been developed for many years. The thermodynamic simulation model of this system is of reference significance for the barocaloric refrigeration system. Dang et al. evaluated the thermodynamic performance of the magnetic refrigeration system using  $\text{MnFeP}_{0.45}\text{As}_{0.55}$  as the refrigerant [41]. Yang et al. compared the thermodynamic performance of different magnetic refrigeration systems using Gd,  $\text{Gd}_{0.95}\text{Dy}_{0.05}$ , or  $\text{Gd}_{0.95}\text{Er}_{0.05}$  as the refrigerants [42].

In order to investigate the energy performance of the barocaloric system with NPG as the refrigerant, a metastable  $T$ - $s$  diagram with phase transformation kinetics of NPG was established using the heat flow data from Lloveras et al.'s article for the first time. On this basis, a reverse Brayton cycle was developed to study the system performance in terms of adiabatic irreversibility, operating temperature, and operating pressure. Still, the optimal system performance was explored by studying the influence of the finite-rate heat transfer of the two isobaric processes on the system performance. More importantly, this paper reflected the development potential of NPG as a barocaloric refrigerant, provided theoretical guidance for the design of barocaloric systems, and proposed future directions for the modification of NPG.

## 2. System Description and Modeling

### 2.1 A metastable temperature-entropy diagram

The material properties studied by Lloveras et al. [36] were used to establish the metastable  $T$ - $s$  diagram for NPG near the phase transition region, as shown in Fig. 1. Combining previous studies on the magnetocaloric effect [14, 43–45] and barocaloric effect [37, 46], the barocaloric effect driven under a pressure change is reversible in thermally anhysteretic regions, e.g., the

region bounded by  $T$ - $s$  ( $p=0$  MPa) on heating and  $T$ - $s$  ( $p=570$  MPa) on cooling (the green highlighted area in Fig. 1). Changes in the adiabatic processes depend on whether the material is applied the pressure for the first time or after repeated cycles, as shown by the arrows in Fig. 1.  $1 \rightarrow 2$  represents an irreversible barocaloric process and  $1r \leftrightarrow 2$  represents a reversible barocaloric process. Based on the content above, a reverse Brayton cycle was established using the cooling  $T(s)_p$  curve at high pressure and the heating  $T(s)_p$  curve at atmospheric pressure.

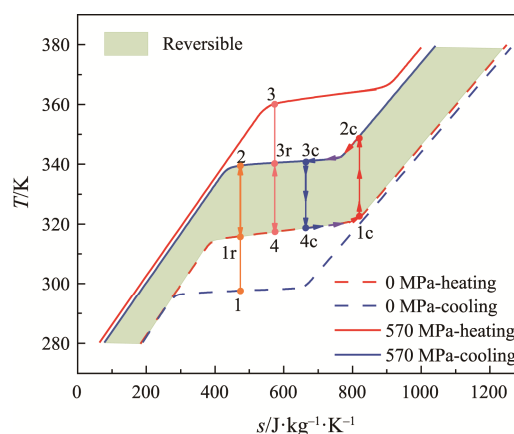
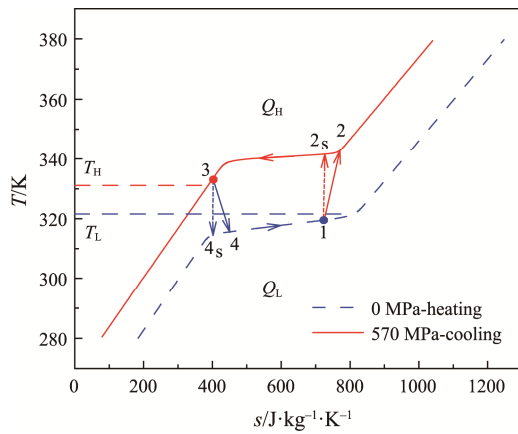


Fig. 1 The  $T$ - $s$  diagram of NPG for cooling and heating processes at 0 MPa and 570 MPa

### 2.2 Reverse Brayton cycle and the related thermodynamic parameters

A reverse Brayton cycle based on the barocaloric effect is consisted of two adiabatic and two isobaric processes, as shown in Fig. 2. The adiabatic compression and expansion processes are established in the thermally anhysteretic regions, which have been verified in the previous studies [14, 30, 37, 44]. The isobaric exothermic and endothermic processes are established based on the data measured by Lloveras et al. [36]. In the first process ( $1 \rightarrow 2$ ), the system is subjected to adiabatic loading, resulting in an increase in the temperature of NPG. When the pressure reaches the setting value, NPG releases heat to the heat sink under the constant operating pressure by the way of heat transfer fluid flowing, as shown in the second process ( $2 \rightarrow 3$ ). In the third process ( $3 \rightarrow 4$ ), the operating pressure is unloaded, causing a decrease in the temperature of NPG. Lastly, as visible in the fourth process ( $4 \rightarrow 1$ ), the heat transfer fluid flowing in the compressor brings the cooling capacity from NPG to the heat source.

$T_H$  is the temperature of the heat sink;  $T_L$  is the temperature of the heat source, and the temperature difference between the two is the temperature span of the barocaloric refrigeration system.



**Fig. 2** The  $T$ - $s$  diagram of a reverse Brayton cycle based on barocaloric effect

According to the thermodynamic cycle established above, the heat exchanged in the two isobaric processes are given respectively by

$$Q_H = \int_{s_3}^{s_2} T ds \quad (1)$$

And

$$Q_L = \int_{s_4}^{s_1} T ds \quad (2)$$

Neglecting the heat loss during the heat transfer process, the mechanical work input  $W$  equals the heat flow out of the system according to the first law of thermodynamics.

$$W = Q_H - Q_L \quad (3)$$

For a real refrigeration system, each process of the cycle is irreversible. The adiabatic compression efficiency and expansion efficiency are introduced to describe the irreversibility of two adiabatic processes referring to the magnetic refrigerator [47].

$$\eta_c = \frac{T_{2s} - T_1}{T_2 - T} \quad (4)$$

And

$$\eta_e = \frac{T_3 - T_4}{T_3 - T_{4s}} \quad (5)$$

where the compressor efficiency ( $\eta_c$ ) and expander efficiency ( $\eta_e$ ) are less than 1.

Due to heat-transfer irreversibility of the two isobaric processes, the temperatures  $T_3$  and  $T_1$  of state-points 3 and 1 are different from the temperatures of heat sink  $T_H$  and the heat source  $T_L$ . In order to compare the refrigeration capacity of the system under different operating conditions, this paper established a heat transfer model referring to the papers of Yang et al. [42] and Xia et al. [47]. The heat transfer between NPG and the heat transfer fluid is assumed to obey the Newtonian law, so  $Q_L$  and  $Q_H$  can be expressed as:

$$Q_H = h_H A_H \Delta T_H t_H \quad (6)$$

and

$$Q_L = h_L A_L \Delta T_L t_L \quad (7)$$

where  $h_H$  and  $h_L$  are the heat transfer coefficients;  $t_H$  and  $t_L$  are the amount of time spent for heat transfer;  $A_H$  and  $A_L$  are the heat transfer areas, and  $\Delta T_H = \frac{\int_3^2 T ds}{s_2 - s_3} - T_H$  and

$\Delta T_L = T_H - \frac{\int_4^1 T ds}{s_1 - s_4}$  are the temperature difference during

heat transfer. The times needed for adiabatic compression and expansion processes are ignored due to no heat exchange. Therefore, the time for a single thermodynamic cycle is that

$$t = t_H + t_L \quad (8)$$

### 2.3 Indexes for thermodynamic performance

For a refrigeration system, the refrigeration capacity and coefficient of performance are two important indexes to evaluate the system performance. Now, using Eqs. (1)–(8), the expressions for the refrigeration capacity and COP for the system can be derived as

$$R = \frac{Q_L}{t} = \frac{h_H h_L A_H A_L \left[ \left( \int_3^2 T ds \right) / (s_2 - s_3) - T_H \right] \left[ T_L - \left( \int_4^1 T ds \right) / (s_1 - s_4) \right] \int_4^1 T ds}{h_L A_L \left[ T_L - \left( \int_4^1 T ds \right) / (s_1 - s_4) \right] \int_3^2 T ds + h_H A_H \left[ \left( \int_3^2 T ds \right) / (s_2 - s_3) - T_H \right] \int_4^1 T ds} \quad (9)$$

$$\text{COP} = \frac{Q_L}{W} = \frac{Q_L}{Q_H - Q_L} \quad (10)$$

Different from the refrigeration capacity commonly used in refrigeration technology, the internal heat transfer mechanism between NPG and heat transfer fluid is not clear. Therefore, the following assumptions are made and the dimensionless refrigeration capacity is introduced. The heat transfer coefficients during the two isobaric

processes are assumed to be the same with reference to an elastocaloric regenerator [48], that is,  $h_L = h_H = h$ . The heat transfer areas are also assumed to be the same since the volume of the solid-state refrigerant varies small, that is,  $A_L = A_H = A$ . This research focuses on the impact of the temperature difference of the heat transfer on the system performance. Therefore, the effect of heat transfer coefficients and areas on the system performance is

ignored, and the dimensionless refrigeration capacity  $R^*$  can be expressed as follows

$$R^* = \frac{R}{h\Delta T_L} = \frac{1}{\frac{Q_H/Q_L}{\Delta T_H} + \frac{1}{\Delta T_L}} \quad (11)$$

### 3. Results and Discussion

#### 3.1 Effect of irreversibility on the performance indexes

The efficiencies of adiabatic compression and expansion are assumed to be the same because these two processes are operated in the same chamber, that is,  $\eta_c = \eta_e = \eta$ . The following content,  $\eta$  is named compressor efficiency. As shown in Fig. 3, the effect of  $\eta$  on the system performance under given operating conditions is investigated. In order to study the optimal performance of the system in different temperature ranges, the heat transfer time of two isobaric processes in the barocaloric refrigeration system was adjusted to achieve optimal operation. According to the previous description, adjusting the heat transfer time was to adjust the heat transfer temperature difference in two isobaric processes. The optimal coefficient of performance ( $\text{COP}_{\max}$ ) and the

optimal dimensionless refrigeration capacity ( $R^*_{\max}$ ) are the optimal performance indexes after system optimization.

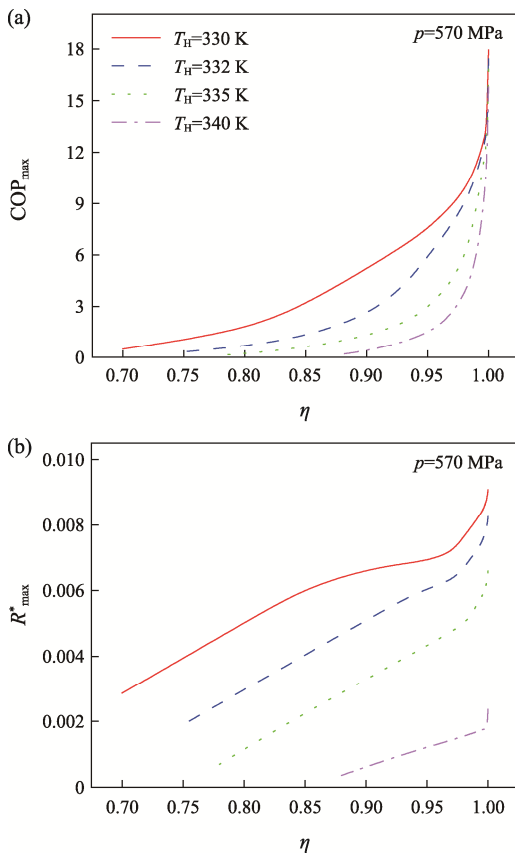
Fig. 3(a) exhibits that  $\text{COP}_{\max}$  increases exponentially with  $\eta$  for all different  $T_H$ . Fig. 3(b) reveals that  $R^*_{\max}$  increases steadily at the beginning as  $\eta$  increases, but sharply as  $\eta$  approaches 1. It is consistent with the fact that the cycle is close to the reverse Carnot cycle when the compressor efficiency was close to 1, which has the maximum COP and refrigeration capacity.

For a vapor compression refrigeration compressor [49], there are pressure losses due to suction and discharge, clearance loss, temperature loss, leakage loss of refrigerant, and friction loss during compression and expansion. The major losses for a barocaloric refrigeration compressor are friction loss and temperature loss. So, it seems that the loss of the barocaloric refrigeration compressor is less than that of the vapor compression refrigeration compressor. Magnetic refrigeration is also a solid-state refrigeration technology, which has been developed for many years. Like barocaloric refrigeration system, its main energy losses are also the temperature loss of the material and the friction loss of the driving device. At the same time, magnetic refrigeration system also adopts the method of indirect heat transfer with the outside world as barocaloric refrigeration. Considering that the compression efficiency of the vapor compression refrigeration system is about 0.85 [50] and the adiabatic efficiency of the magnetic refrigerator is 0.95 [47, 51, 52], a compressor efficiency of 0.95 is assumed for the barocaloric refrigeration in the following work. An uncertainty of 10%–20% exists in the assumption of the adiabatic efficiency due to differences between the barocaloric refrigerator drive and the magnetic refrigerator, which will be verified by subsequent experiments.

#### 3.2 Effect of operating temperature range

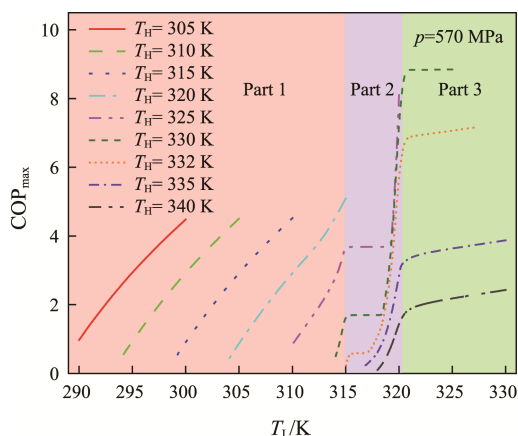
##### 3.2.1 Effect of operating temperature range on the $\text{COP}_{\max}$

Fig. 4 illustrates the effect of operating temperature range on the  $\text{COP}_{\max}$ , which is separated into three parts. Part 1 (pink highlighted area) indicates that  $\text{COP}_{\max}$  increases with  $T_L$ , where the system is operating in the non-phase transition region. This is because  $\text{COP}_{\max}$  is proportional to the temperature difference between the heat sink and heat source under this case. Part 2 (purple highlighted area) can be divided into a section with a constant  $\text{COP}_{\max}$  and a section with a sharp increase in  $\text{COP}_{\max}$ , where the system is operating in the phase transition region. Since the compressor efficiency in this paper is based on temperature, the temperature increases greatly with entropy in the non-phase transition region,



**Fig. 3** The effect of compressor efficiency on (a)  $\text{COP}_{\max}$  and (b)  $R^*_{\max}$  when  $T_L = 320$  K and  $p = 570$  MPa

and is relatively stable in the phase transition region. The effect of the compressor efficiency on COP is great when the system is operating in the initial stage of the phase transition, and small when the operating temperature range contains the phase transition region. In addition, considering the large thermal hysteresis of neopentyl glycol, problems such as state instability may occur when the system is operated in this part, resulting in a low efficiency. Part 3 (green highlighted area) shows that  $COP_{max}$  increases gradually with  $T_L$ , where the operating temperature range contains the entire phase transition region. Under this condition, COP is at a high value and increases with the decrease of the temperature difference. Fig. 5 analyzes the effect of the temperature difference during heat transfer on the performance within a given operating temperature range.



**Fig. 4** Effect of operating temperature range on the  $COP_{max}$

The previous formulas show that COP is determined by thermodynamic cycles and can be optimized by adjusting the temperature differences of heat transfer within the given operating temperature range. Taking the operating temperature range of  $T_H=330$  K,  $T_L=325$  K as an example, Fig. 5(a) shows the distribution of COP affected by both  $T_1$  and  $T_3$ , and Fig. 5(b) illustrates different thermodynamic cycles corresponding to Fig. 5(a). In order to better understand the influence of the phase transition region on the system performance, four points of phase transition are marked on the  $T$ - $s$  diagram in Fig. 5(b). The cycles operate in the non-phase transition region when  $T_1$  is less than 315 K from Fig. 5(a). Under this condition,  $Q_H/Q_L$  decreases with the temperature difference between  $T_1$  and  $T_3$ , leading to the increase in COP. When the temperature  $T_2$  of state-point 2 is close to the 1st phase transition temperature  $T_{1st}$ , COP is affected heavily by the compressor efficiency. As shown in Fig. 5(b), the value of  $Q_H/Q_L$  increases sharply when the compression process changes from  $b1 \rightarrow b2$  to  $d1 \rightarrow d2$ , resulting in a rapid decrease in COP. Then, COP increases steadily with  $T_1$  when  $T_2$  is still smaller than the

2nd phase transition temperature  $T_{2nd}$ . When  $T_2$  is close to  $T_{2nd}$ , COP increases rapidly due to the sharp decrease of  $Q_H/Q_L$ .

In order to better summarize the optimal operating conditions for NPG, the  $T$ - $s$  diagram of NPG is divided into five regions, as shown in Fig. 6. When the operating temperature range includes Regions 2 and 3, that is,

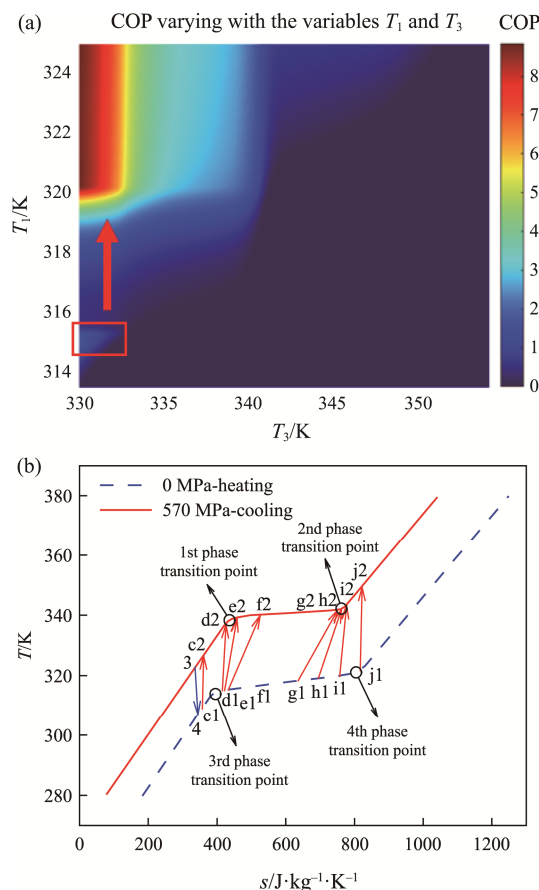


**Fig. 5** (a) Distribution map of COP and (b) thermodynamic cycles when  $T_H=330$  K and  $T_L=325$  K

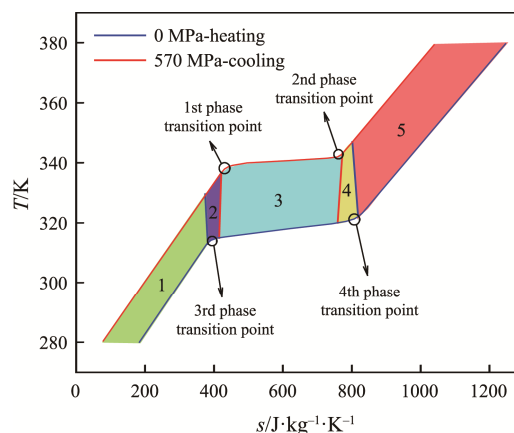


**Fig. 6** Different regions in the  $T$ - $s$  diagram using NPG as refrigerant



including the 2nd and 3rd phase transition points, a maximum COP of 8.8 and corresponding temperature span of 10 K can be achieved. Nevertheless, the high operating temperature range will limit the application of NPG in conventional refrigeration. When the system operates at room temperature, that is, in Region 1, a maximum COP of 3 and a corresponding temperature span of 10 K can be achieved. The performance of the barocaloric system using NPG under this operating temperature range is still considerable, but it is inferior to that of vapor compression refrigeration systems.

### 3.2.2 Effect of operating temperature range on $R^*_{\max}$

Fig. 7 represents the variation of the optimal dimensionless refrigeration capacity ( $R^*_{\max}$ ) under different operating temperature ranges, divided into three parts corresponding to Fig. 4. Part 1 (pink highlighted area) shows a linearly increasing relationship between  $R^*_{\max}$  and  $T_L$  when the system is operated in the non-phase transition region. Part 2 (purple highlighted area) displays that  $R^*_{\max}$  still rises with  $T_L$ , but not linearly. When the system is operated in Part 3 (green

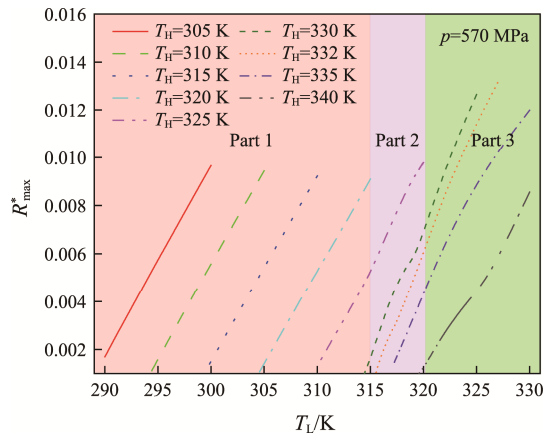


Fig. 7 Effect of operating temperature range on the  $R^*_{\max}$

highlighted area), the maximum  $R^*_{\max}$  can be achieved is about 1.3 times that in Part 1. Figs. 8 and 9 analyze the factors affecting the  $R^*$  under different given operating temperature ranges. According to Eq. (9),  $R^*$  is optimized by adjusting the heat release ( $Q_L$ ) and the time required for a cycle ( $t$ ).

Fig. 8 represents the dimensionless refrigeration capacity ( $R^*$ ) of the barocaloric systems under different operating temperature ranges in Part 1 (see Fig. 7). The distribution maps show that  $R^*$  always takes the maximum value when  $T_1 = T_L$  and  $T_3 = T_H$ . In Part 1, the temperature difference of heat transfer in the exothermic and endothermic processes was relatively large, so the times required for heat transfer were short, resulting in a relatively small effect on  $R^*$ . So, the variation of  $Q_H/Q_L$  under this condition was the main reason for the effect of  $R^*$ . The decrease in  $Q_H/Q_L$  indicated a larger share of  $Q_L$  and a smaller share of  $t_H$  in a single cycle, resulting in an improvement in the refrigeration capacity. In addition, it can be observed from Figs. 7 and 8 that  $R^*_{\max}$  trended upward as the temperature span of the system decreases, which was also subject to the influence of  $Q_H/Q_L$ .

Fig. 9 shows the distribution of  $R^*$  under operating temperature ranges in Parts 2 and 3. Combining Fig. 9 and Fig. 5(a), it can be found that the distribution of  $R^*$  is similar to that of COP under the same operating temperature range. In Parts 2 and 3,  $Q_H/Q_L$  is still the main factor influencing  $R^*$ , but the influence of heat transfer time of the system cannot be ignored due to the large difference in the temperature difference of heat transfer. It can be seen from Fig. 9(b),  $R^*$  cannot get maximum when  $T_1 = T_L$  and  $T_3 = T_H$  like  $COP_{\max}$ . The time for the exothermic process  $t_L$  needs to be reduced by increasing the temperature difference of heat transfer  $\Delta T_L$  to improve the refrigeration capacity. In addition,  $R^*$  is achieved an extreme value when  $T_2$  reaches the 2nd

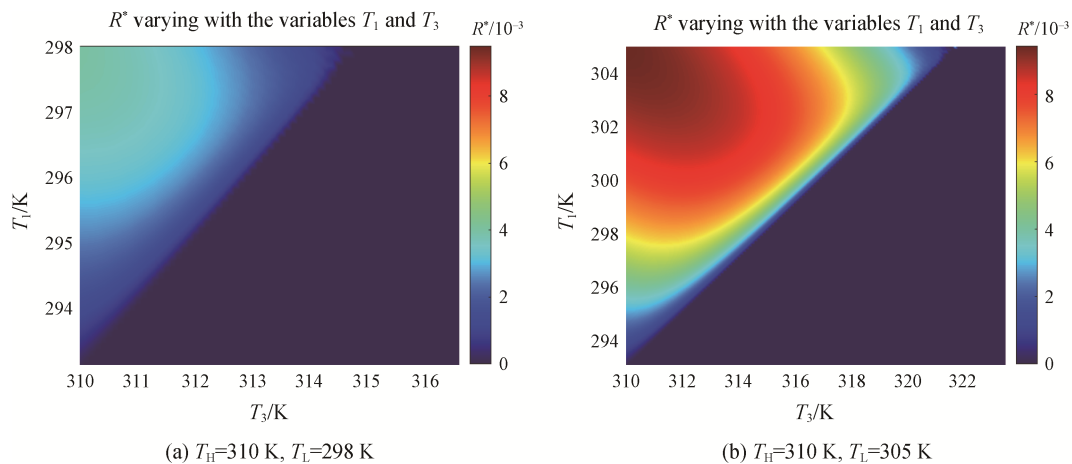


Fig. 8 Distribution maps of  $R^*$  under different operating temperature ranges in Part 1

phase transition point due to the variation of  $Q_H/Q_L$ . Different from  $COP_{max}$ , the extreme value increases with the temperature of the heat source, as shown in Part 2 of Fig. 7.

Based on the analysis of  $R^*$ , it is found that the optimal cycle corresponding to  $R^*_{max}$  under the same operating condition is like that of  $COP_{max}$ .  $Q_H/Q_L$  is still the main factor influencing  $R^*$ . In order to obtain the optimal performance under the given operating temperature range, the thermodynamic cycle corresponding to  $COP_{max}$  should be determined firstly, and then the temperature

differences of heat transfer in two isobaric processes should be adjusted to enhance the refrigeration capacity.

### 3.3 Effect of the operating pressure

Due to a large hysteresis effect of NPG, it is necessary to use an operating pressure of at least 190 MPa to overcome the hysteresis. According to the  $T$ - $s$  diagram of NPG, several operating pressures of 250 MPa, 290 MPa, 350 MPa and 570 MPa were selected to investigate their effect on the performance of barocaloric system. The research in this chapter is developed at the same heat

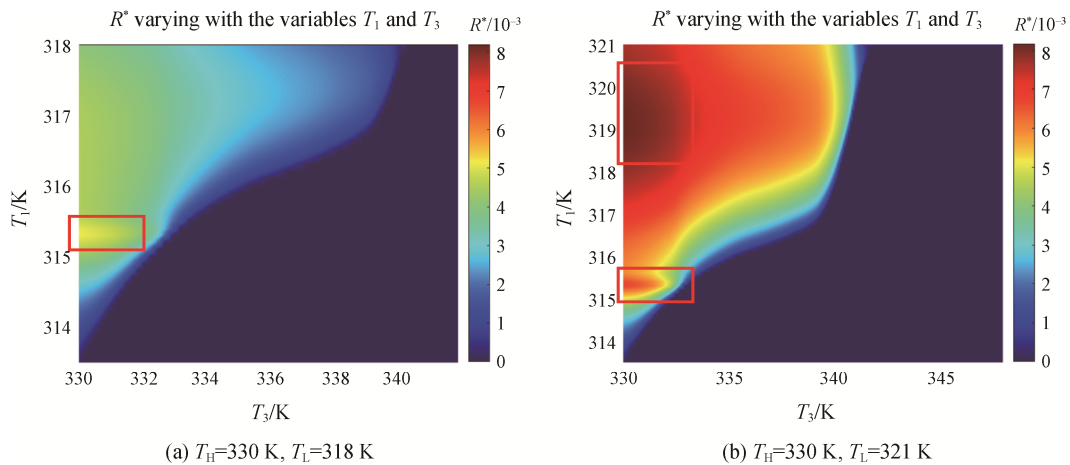


**Fig. 9** Distribution maps of  $R^*$  under different operating temperature ranges in Parts 2 and 3

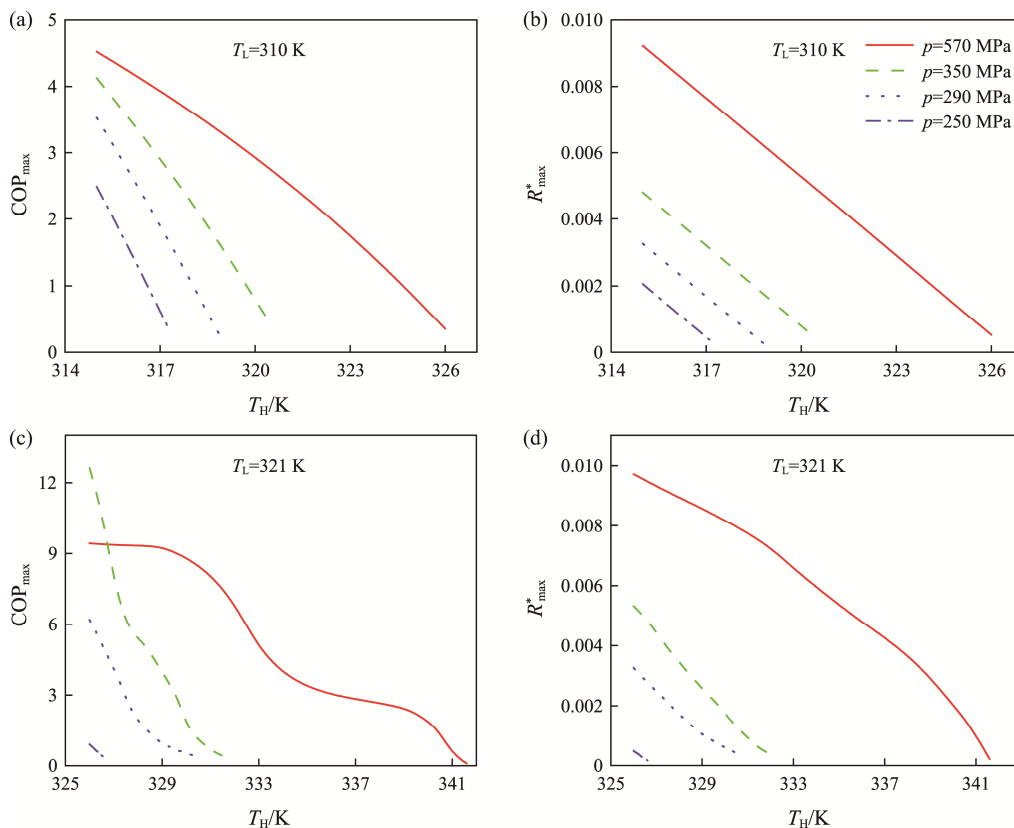


**Fig. 10** Comparison of  $COP_{max}$  and  $R^*_{max}$  under different operating pressures (a) (b) at  $T_L=310$  K (c) (d) at  $T_L=321$  K



source temperatures since the cycles under different operating pressures share the heating  $T(s)_P$  curve at atmospheric pressure.

Figs. 10(a) and 10(b) represent the performances of the cycles operating in Region 1 (see Fig. 7). Both  $COP_{max}$  and  $R^*_{max}$  increase with the rise of operating pressure under the same operating temperature range. However, with the increase of heat sink temperature,  $COP_{max}$  of the cycle with lower operating pressure in Fig. 10(a) decreases rapidly, while the variation trend of  $R^*_{max}$  under different operating pressures in Fig. 10(b) is roughly the same. In addition, the maximum temperature span of the system increases with the operating pressure. Figs. 10(c) and 10(d) show the performances of the cycles operating in Region 2, 3, and 4. Different from the cycles operating in Region 1,  $COP_{max}$  at 570 MPa is smaller than that at 350 MPa when  $T_H$  is lower than 326.7 K, and the variation trend is reversed when  $T_H$  is larger than 326.7 K. According to the analysis of Fig. 5 (b), cycles corresponding to  $COP_{max}$  are always at  $T_3=T_H$  and  $T_1=T_L$  when  $T_L=321$  K and  $T_H$  is larger than 326 K. For better understanding, the cycles under these operating pressures are represented in Fig. 11. It can be seen that  $T_3$  in the cycles at 570 MPa and 350 MPa is smaller than  $T_{3rd}$  when  $T_H=326$  K, and the variation trend can refer to the Carnot cycle. With the increase of  $T_H$ ,  $T_3$  in the cycle at 350 MPa reaches the first phase transition point early and  $COP_{max}$  will begin to decrease sharply. In addition, the variation trends of  $R^*_{max}$  are almost the same, which indicates that the main factors affecting  $R^*_{max}$  are the operating temperature range and the operating pressure.

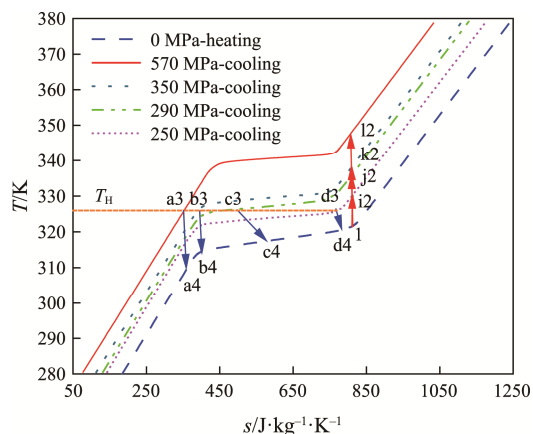


**Fig. 11** Thermodynamic cycles corresponding to  $COP_{max}$  under different operating pressures at  $T_L=321$  K and  $T_H=326$  K

Based on the above study, it is found that the barocaloric system using NPG requires an operating pressure of at least 250 MPa to realize refrigeration. In general cases, the achievable performance and temperature span of the system increase with the rise of operating pressure. In addition, it is necessary to make a

judgment whether the 3rd phase transition point is within the operating temperature range when the optimal operating pressure is designed.

#### 4. Conclusions

This investigation of this paper is concentrated on the determination of the performances of the barocaloric system using Neopentyl glycol as the refrigerant. A reverse Brayton cycle is established based on the metastable  $T-s$  diagram for the first time, and the performances are investigated in terms of different operating conditions. The optimal system performance is explored by studying the influence of the finite-rate heat transfer of the two isobaric processes on the system performance. Based on the investigation, the potential of Neopentyl glycol as a barocaloric refrigerant is analyzed and the guidance for the design of the barocaloric system is provided. The following conclusions can be drawn.

(1) A maximum COP of 8.8 and a corresponding temperature span of 10 K can be achieved by making full use of the phase transition region of Neopentyl glycol. However, the operating temperature range is too high and not suitable for common refrigeration applications. A COP of 3 and the corresponding temperature span of 10 K can be achieved when the system operates at room temperature, which is common and inferior to the performance of vapor compression refrigeration systems.

(2) In order to design a barocaloric system with optimal performances under a given operating temperature range, the thermodynamic cycle corresponding to  $COP_{max}$  should be determined firstly, and then the temperature difference of heat transfer in two isobaric processes should be adjusted to enhance the refrigeration capacity.

(3) The barocaloric system using Neopentyl glycol requires an operating pressure of at least 250 MPa to realize refrigeration. In addition, the performance of the system increases with the operating pressure in general cases, and a maximum temperature span of 20 K can be achieved at 570 MPa. Moreover, the relationship between the third phase transition point and the operating temperature range is a matter of concern when the optimal operating pressure is designed.

It is found from the investigation that the system performance using Neopentyl glycol is outstanding when the system fully uses the phase transition region of Neopentyl glycol, but the operating temperature range is high. In addition, the operating pressure is too high. In order to improve the energy performance of Neopentyl glycol, the following suggestions are given.

(1) By adding different plastic crystals to neopentyl glycol, polyols with adjustable phase transition temperature were prepared by high temperature melting

method, such as pentaerythritol, trimethylolethane, trimethylolpropane.

(2) Choosing a suitable nucleating agent and combining it with Neopentyl glycol can reduce the thermal hysteresis of the refrigerant to lower the minimum operating pressure of the barocaloric system.

## Acknowledgments

The research described in this research is supported by the Basic Research Program of Frontier Leading Technologies in Jiangsu Province (BK20202008), Hebei Natural Science Foundation (No. E2022210022), Science and Technology Project of Hebei Education Department (No. BJK2022056) and the Introduction Program of Oversea Talents of Hebei Province (No. C20220505).

## References

- [1] Edith Molenbroek M.S., Nesen S., Sven S., et al., Savings and benefits of global regulations for energy efficient products. European Commission, 2015.
- [2] Heredia-Aricapa Y., Belman-Flores J.M., Mota-Babiloni A., et al., Overview of low GWP mixtures for the replacement of HFC refrigerants: R134a, R404A and R410A. *International Journal of Refrigeration*, 2020, 111: 113–123.
- [3] Arpagaus C., Bless F., Uhlmann M., et al., High temperature heat pumps: Market overview, state of the art, research status, refrigerants, and application potentials. *Energy*, 2018, 152: 985–1010.
- [4] Wu D., Hu B., Wang R.Z., Vapor compression heat pumps with pure Low-GWP refrigerants. *Renewable & Sustainable Energy Reviews*, 2021, 138: 110571.
- [5] Kitanovski A., Plaznik U., Tomc U., Poredos A., Present and future caloric refrigeration and heat-pump technologies. *International Journal of Refrigeration-Revue Internationale Du Froid*, 2015, 57: 288–298.
- [6] Shi X.L., Zou J., Chen Z.G., Advanced thermoelectric design: from materials and structures to devices. *Chemical Reviews*, 2020, 120(15): 7399–7515.
- [7] Franco V., Blazquez J.S., Ipus J.J., et al., Magnetocaloric effect: From materials research to refrigeration devices. *Progress in Materials Science*, 2018, 93: 112–232.
- [8] Shi J., Han D., Li Z., et al., Electrocaloric cooling materials and devices for zero-global-warming-potential, high-efficiency refrigeration. *Joule*, 2019, 3(5): 1200–1225.
- [9] Qian S., Geng Y., Wang Y., et al., A review of elastocaloric cooling: Materials, cycles and, system integrations. *International Journal of Refrigeration-Revue Internationale Du Froid*, 2016, 64: 1–19.
- [10] Li B., Kawakita Y., Ohira-Kawamura S., et al., Colossal barocaloric effects in plastic crystals. *Nature*, 2019, 567(7749): 506–510.
- [11] Zhou Y., Yu J., Design optimization of thermoelectric cooling systems for applications in electronic devices. *International Journal of Refrigeration*, 2012, 35(4): 1139–1144.
- [12] Zhao D., Tan G., A review of thermoelectric cooling: Materials, modeling and applications. *Applied Thermal Engineering*, 2014, 66(1–2): 15–24.
- [13] Brück E., Tegus O., Li X.W., et al., Magnetic refrigeration—towards room-temperature applications. *Physica B: Condensed Matter*, 2003, 327(2–4): 431–437.
- [14] Gottschall T., Skokov K.P., Fries M., et al., Making a cool choice: the materials library of magnetic refrigeration. *Advanced Energy Materials*, 2019, 9(34): 1901322.
- [15] Gschneidner K.A., Pecharsky V.K., Thirty years of near room temperature magnetic cooling: Where we are today and future prospects. *International Journal of Refrigeration*, 2008, 31(6): 945–961.
- [16] Shi J., Li Q., Gao T., et al., Numerical evaluation of a kilowatt-level rotary electrocaloric refrigeration system. *International Journal of Refrigeration*, 2021, 121: 279–288.
- [17] Nair B., Usui T., Crossley S., et al., Large electrocaloric effects in oxide multilayer capacitors over a wide temperature range. *Nature*, 2019, 575(7783): 468–472.
- [18] Ožbolt M., Kitanovski A., Tušek J., Poredoš A., Electrocaloric vs. magnetocaloric energy conversion. *International Journal of Refrigeration*, 2014, 37: 16–27.
- [19] Guo M., Sun B., Wu M., et al., Effect of polarization fatigue on the electrocaloric effect of relaxor  $\text{Pb}_{0.92}\text{La}_{0.08}\text{Zr}_{0.65}\text{Ti}_{0.35}\text{O}_3$  thin film. *Applied Physics Letters*, 2020, 117(20): 202901.
- [20] Chen J., Lei L., Fang G., Elastocaloric cooling of shape memory alloys: A review. *Materials Today Communications*, 2021, 28: 102706.
- [21] Greibich F., Schwödiauer R., Mao G., et al., Elastocaloric heat pump with specific cooling power of 20.9 W g<sup>-1</sup> exploiting snap-through instability and strain-induced crystallization. *Nature Energy*, 2021, 6(3): 260–267.
- [22] Qian S., Alabdulkarem A., Ling J., et al., Performance enhancement of a compressive thermoelastic cooling system using multi-objective optimization and novel designs. *International Journal of Refrigeration*, 2015, 57: 62–76.
- [23] Manosa L., Planes A., Materials with giant mechanocaloric effects: cooling by strength. *Advanced Materials*, 2017, 29(11): 1–25.
- [24] Manosa L., Gonzalez-Alonso D., Planes A., et al., Giant solid-state barocaloric effect in the Ni-Mn-In magnetic shape-memory alloy. *Nature Materials*, 2010, 9(6): 478–481.
- [25] Manosa L., Gonzalez-Alonso D., Planes A., et al., Inverse

- barocaloric effect in the giant magnetocaloric La-Fe-Si-Co compound. *Nature Communications*, 2011, 2: 595.
- [26] Yuce S., Barrio M., Emre B., et al., Barocaloric effect in the magnetocaloric prototype  $\text{Gd}_5\text{Si}_2\text{Ge}_2$ . *Applied Physics Letters*, 2012, 101(7): 071906.
- [27] Stern-Taulats E., Planes A., Lloveras P., et al., Barocaloric and magnetocaloric effects in  $\text{Fe}_{49}\text{Rh}_{51}$ . *Physical Review B*, 2014, 89(21): 214105.
- [28] Matsunami D., Fujita A., Takenaka K., Kano M., Giant barocaloric effect enhanced by the frustration of the antiferromagnetic phase in  $\text{Mn}_3\text{GaN}$ . *Nature Materials*, 2015, 14(1): 73–78.
- [29] Bermúdez-García M.J., Sánchez-Andújar M., Castro-García S., et al., Giant barocaloric effect in the ferroic organic-inorganic hybrid  $[\text{TPrA}][\text{Mn}(\text{dca})_3]$  perovskite under easily accessible pressures. *Nature Communications*, 2017, 8(1): 15715.
- [30] Aznar A., Lloveras P., Romanini M., et al., Giant barocaloric effects over a wide temperature range in superionic conductor  $\text{AgI}$ . *Nature Communications*, 2017, 8(1): 1851.
- [31] Romanini M., Wang Y., Gurbinar K., et al., Giant and reversible barocaloric effect in trinuclear spin-crossover complex  $\text{Fe}_3(\text{bntz})_6(\text{tenset})_6$ . *Advanced Materials*, 2021, 33(10): e2008076.
- [32] Kosugi Y., Goto M., Tan Z., et al., Colossal barocaloric effect by large latent heat produced by first-order intersite-charge-transfer transition. *Advanced Functional Materials*, 2021.
- [33] Boldrin D., Fantastic barocalorics and where to find them. *Applied Physics Letters*, 2021, 118(17): 170502.
- [34] Lloveras P., Tamarit J.-L., Advances and obstacles in pressure-driven solid-state cooling: A review of barocaloric materials. *Mrs Energy & Sustainability*, 2021.
- [35] Li F. B., Li M., Xu X., et al., Understanding colossal barocaloric effects in plastic crystals. *Nature Communications*, 2020, 11(1): 4190.
- [36] Lloveras P., Aznar A., Barrio M., et al., Colossal barocaloric effects near room temperature in plastic crystals of neopentylglycol. *Nature Communications*, 2019, 10(1): 1803.
- [37] Aznar A., Lloveras P., Barrio M., et al., Reversible and irreversible colossal barocaloric effects in plastic crystals. *Journal of Materials Chemistry A*, 2020, 8(2): 639–647.
- [38] Aprea C., Greco A., Maiorino A., Masselli C., Solid-state refrigeration: A comparison of the energy performances of caloric materials operating in an active caloric regenerator. *Energy*, 2018, 165: 439–455.
- [39] Aprea C., Greco A., Maiorino A., Masselli C., The use of barocaloric effect for energy saving in a domestic refrigerator with ethylene-glycol based nanofluids: A numerical analysis and a comparison with a vapor compression cooler. *Energy*, 2020, 190: 116404.
- [40] Takenaka K., Sugiura T., Kadowaki Y., et al., Giant Magneto-volume and Magneto-caloric effects of frustrated antiferromagnet  $\text{Mn}_3\text{GaN}$  under hydrostatic pressure. *Journal of the Physical Society of Japan*, 2021, 90(4): 044601.
- [41] Liqing Dang X.Z., Yan Li, Zhiming Yang, Guoxing Lin, Performance Analysis of the Thermodynamic Cycle Using the Refrigeration Material  $\text{MnFeP}_{0.45}\text{As}_{0.55}$  as the Working Substance. *Journal of Engineering Thermophysics*, 2019, 40(7): 1470–1475.
- [42] Yang Z., Xu Z., Wang J., et al., Thermoeconomic performance optimization of an irreversible Brayton refrigeration cycle using Gd,  $\text{Gd}_{0.95}\text{Dy}_{0.05}$  or  $\text{Gd}_{0.95}\text{Er}_{0.05}$  as the working substance. *Journal of Magnetism and Magnetic Materials*, 2020, 499: 166189.
- [43] Gutfleisch O., Gottschall T., Fries M., et al., Mastering hysteresis in magnetocaloric materials. *Philosophical Transactions of the Royal Society A*, 2016, 374: 20150308.
- [44] Gottschall T., Stern-Taulats E., Mañosa L., et al., Reversibility of minor hysteresis loops in magnetocaloric Heusler alloys. *Applied Physics Letters*, 2017, 110(22): 223904.
- [45] Skokov K.P., Müller K.H., Moore J.D., et al., Influence of thermal hysteresis and field cycling on the magnetocaloric effect in  $\text{LaFe}_{11.6}\text{Si}_{1.4}$ . *Journal of Alloys and Compounds*, 2013, 552: 310–317.
- [46] Stern-Taulats E., Gracia-Condal A., Planes A., et al., Reversible adiabatic temperature changes at the magnetocaloric and barocaloric effects in  $\text{Fe}_{49}\text{Rh}_{51}$ . *Applied Physics Letters*, 2015, 107(15): 152409.
- [47] Xia Z., Zhang Y., Chen J., Lin G., Performance analysis and parametric optimal criteria of an irreversible magnetic Brayton-refrigerator. *Applied Energy*, 2008, 85(2–3): 159–170.
- [48] Tušek J., Engelbrecht K., Eriksen D., et al., A regenerative elastocaloric heat pump. *Nature Energy*, 2016, 1(10): 16134.
- [49] Bell I.H., Groll E.A., Braun J.E., Performance of vapor compression systems with compressor oil flooding and regeneration. *International Journal of Refrigeration*, 2011, 34(1): 225–233.
- [50] She X., Yin Y., Zhang X., A proposed subcooling method for vapor compression refrigeration cycle based on expansion power recovery. *International Journal of Refrigeration*, 2014, 43: 50–61.
- [51] Chen L.G., Sun F.R., Wu C., Kiang R.L., Theoretical analysis of the performance of a regenerative closed Brayton cycle with internal irreversibilities. *Energy Conversion and Management*, 1997, 38(9): 871–877.
- [52] Wang H., Wu G.X., Ecological optimization for an irreversible magnetic Ericsson refrigeration cycle. *Chinese Physics B*, 2013, 22(8): 087501.